EUROPEAN ORGANIZATION FOR NUCLEAR RESEARCH

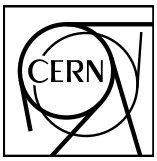

CERN-EP-2022-286
16 December 2022

Production of pions, kaons and protons as a function of the transverse event activity in pp collisions at $\sqrt{s} = 13$ TeV

ALICE Collaboration

Abstract

The production of $\pi^{\pm}$, $\mathrm{K}^{\pm}$, and $(\overline{\mathrm{p}})\mathrm{p}$ is measured in pp collisions at $\sqrt{s} = 13$ TeV in different topological regions of the events. Particle transverse momentum (p_{T}) spectra are measured in the "toward", "transverse", and "away" angular regions defined with respect to the direction of the leading particle in the event. While the toward and away regions contain the fragmentation products of the near-side and away-side jets, respectively, the transverse region is dominated by particles from the Underlying Event (UE). The relative transverse activity classifier, $R_{\mathrm{T}} = N_{\mathrm{T}}/\langle N_{\mathrm{T}} \rangle$, is used to group events according to their UE activity, where N_{T} is the measured charged-particle multiplicity per event in the transverse region and $\langle N_{\mathrm{T}} \rangle$ is the mean value over all the analysed events. The first measurements of identified particle p_{T} spectra as a function of R_{T} in the three topological regions are reported. It is found that the yield of high transverse momentum particles relative to the R_{T}-integrated measurement decreases with increasing R_{T} in both the toward and the away regions, indicating that the softer UE dominates particle production as R_{T} increases and validating that R_{T} can be used to control the magnitude of the UE. Conversely, the spectral shapes in the transverse region harden significantly with increasing R_{T}. This hardening follows a mass ordering, being more significant for heavier particles. Finally, it is observed that the p_{T}-differential particle ratios $(\mathrm{p}+\overline{\mathrm{p}})/(\pi^{+}+\pi^{-})$ and $(\mathrm{K}^{+}+\mathrm{K}^{-})/(\pi^{+}+\pi^{-})$ in the low UE limit ($R_{\mathrm{T}} \to 0$) approach expectations from Monte Carlo generators such as PYTHIA 8 and EPOS LHC, where the jet-fragmentation models have been tuned to reproduce $\mathrm{e}^{+}\mathrm{e}^{-}$ results.

1 Introduction

In recent years, proton–proton (pp) and proton–lead (p–Pb) collisions, commonly denoted as small collision systems, have attracted the heavy-ion community's attention due to several measurements in high-multiplicity pp and p–Pb collisions, which show similar features as those observed in heavy-ion collisions. Observations of radial [1–4] and anisotropic [5, 6] flows (collective phenomena), as well as strangeness enhancement [1, 7, 8] in heavy-ion collisions, are associated with the formation of the strongly interacting quark–gluon plasma (QGP). However, these signatures have also been observed in pp and p–Pb collisions [2, 4, 8, 9]. In particular, the p_{T}-differential baryon-to-meson ratios in small collision systems showcase radial-flow like effects when studied as a function of the charged particle multiplicity of the event [2, 3]. In order to pin down the origins of the effects observed in small collision systems, it has been proposed to study particle production as a function of the Underlying Event (UE) activity [10]. The UE is commonly understood as the collection of particles produced in hadronic collisions that do not originate from the fragmentation products of the partons produced in the hardest scattering. In models such as PYTHIA [11] or Herwig [12, 13], the UE is composed of particles arising from the proton break-up (beam remnants), and from semi-hard multiple parton interactions (MPI). In the context of MPI models, the measurement of identified particle yields and ratios as a function of the UE activity allows one to measure event properties in an MPI-suppressed (-enhanced) environment. Moreover, as shown in [14], these measurements can also provide insights into possible effects that give similar signatures as radial flow but are produced by jet hardening with increasing multiplicity.

At the LHC energies, particles and anti-particles are produced in equal amounts [15]. In the remaining of this paper and unless stated otherwise, the notation π, K and p is adopted to refer to $(\pi^+ + \pi^-)$, $(\mathrm{K}^+ + \mathrm{K}^-)$, and $(\mathrm{p} + \overline{\mathrm{p}})$, respectively. In this study, the production of π, K, and p is studied as a function of the UE activity in pp collisions at centre-of-mass energy, $\sqrt{s} = 13$ TeV. The UE is examined using the event topology defined by the leading particle in the event, which is defined as the charged particle with the highest transverse momentum in the range $5 \leq p_{\mathrm{T}}^{\mathrm{leading}} < 40$ GeV/c, and reconstructed in the pseudorapidity interval $|\eta| < 0.8$. The lower $p_{\mathrm{T}}^{\mathrm{leading}}$ threshold corresponds to the onset of the UE plateau in the transverse region (transverse to the direction of the leading particle) [16]. In the plateau region, quantities such as the charged-particle density, N_{ch}, and the transverse momentum sum, $\sum p_{\mathrm{T}}$, have little dependence on the p_{T} of the leading particle or jet, albeit a slow rise of the UE plateau has been observed. This slow rise can be explained by additional contributions from wide-angle radiation associated with the hard scattering. Since wide-angle contamination becomes significant for jet $p_{\mathrm{T}} > 50$ GeV/c [17], an upper limit on $p_{\mathrm{T}}^{\mathrm{leading}}$ of 40 GeV/c is used to reduce its effects.

To study the particle production associated with different underlying physics mechanisms, the conventional division of the azimuthal (φ) plane into regions relative to the direction of the leading particle [18] is used (see Fig. 1). The observables reported in this paper are measured in three different topological regions, the toward, transverse, and away regions. These are defined based on the absolute difference in azimuthal angle between the leading and associated particles, $|\Delta\varphi| = |\varphi^{\mathrm{leading}} - \varphi|$. The associated particles are measured in the kinematic range $0.15 \leq p_{\mathrm{T}} < 5$ GeV/c and $|\eta| < 0.8$. The toward, transverse, and away regions are defined by $|\Delta\varphi| < 60^\circ$, $60^\circ \leq |\Delta\varphi| < 120^\circ$, and $|\Delta\varphi| \geq 120^\circ$, respectively. The particle production in the toward and away regions contains the constituents of the leading and away-side jets, respectively, the transverse region is mainly sensitive to multiple parton interactions and initial- and final-state radiations.

The UE activity is quantified using the relative transverse activity classifier R_{T} [10], which is defined as $N_{\mathrm{T}}/\langle N_{\mathrm{T}} \rangle$, where N_{T} is the measured charged-particle multiplicity per event in the transverse region and $\langle N_{\mathrm{T}} \rangle$ is the mean value over all the analysed events. By construction, R_{T} cleanly separates events with "higher-than-average" UE from "lower-than-average" ones irrespective of the centre-of-mass energy. Of particular interest is whether events with very low UE activity, which are dominated by the jet activity, exhibit particle ratios and spectra consistent with fragmentation models tuned to $\mathrm{e}^+\mathrm{e}^-$ data and whether

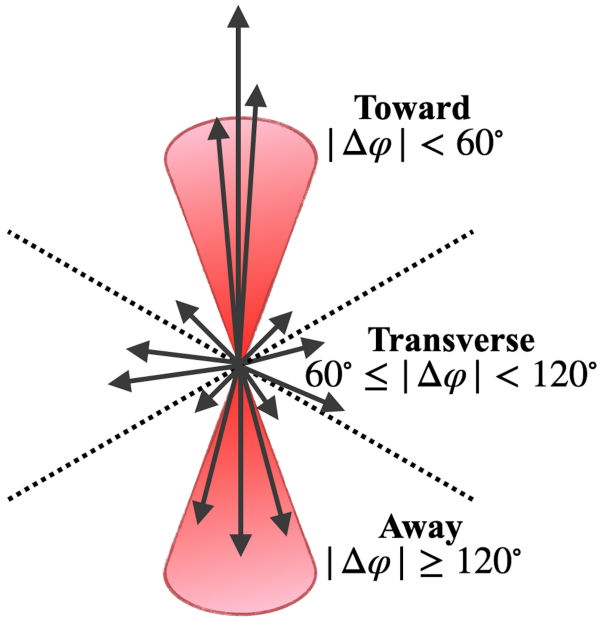

Figure 1: Illustration of the toward, transverse, and away regions in the azimuthal angle plane with respect to the direction of the leading particle. The leading particle is represented with the longest upright arrow. The UE is represented with the small arrows transverse to the leading particle. The red cones represent the jet and away-side jet.

high-UE events exhibit any clear signs of flow or other collective effects [10]. Finally, it is worth mentioning that this study is complementary to the measurements made using transverse spherocity, in which global event properties are studied for jet-like and isotropic topologies [19][20].

The structure of the paper is as follows: In Sec. 2, the data analysis is described, Sec. 3 discusses the systematic uncertainties, and in Sec. 4, the results are presented. Finally, in Sec. 5, the conclusions are given.

2 Analysis procedure

2.1 Event and track selection

This study was carried out with the data collected in pp collisions at $\sqrt{s} = 13$ TeV by the ALICE Collaboration during the LHC runs from 2016 and 2018. A detailed description of the ALICE apparatus and its performance can be found in [21, 22]. The subdetectors used in this analysis are the V0 [23], the Inner Tracking System (ITS) [24], the Time Projection Chamber (TPC) [25], and the Time-Of-Flight (TOF) [26]. These subdetectors are located inside a $B = 0.5$ T solenoidal magnetic field. The V0 detector consists of two arrays of 32 scintillators each, covering the forward (V0A, $2.8 < \eta < 5.1$) and backward (V0C, $-3.7 < \eta < -1.7$) pseudorapidity regions. The ITS is the innermost barrel detector. It consists of six cylindrical layers of high-resolution silicon tracking detectors: the two innermost layers of the Silicon Pixel Detector (SPD) provide a digital readout and are also used as a trigger detector. The Silicon Drift Detector (SDD) and the Silicon Strip Detector (SSD) compose the four outer layers of the ITS. Together, they provide the amplitude of the charge signal, which is used for particle identification through the measurement of the specific energy loss ($\mathrm{d}E/\mathrm{d}x$). The TPC is the primary detector for tracking and particle identification. It is a large cylindrical drift detector with a diameter and length of about 5 m, which covers the pseudorapidity range $|\eta| < 0.8$ with full-azimuth coverage. Particle identification is accomplished via the measurement of the $\mathrm{d}E/\mathrm{d}x$. In pp collisions the resolution of the $\mathrm{d}E/\mathrm{d}x$ is about 5 %. The TOF is a large-area array of multigap resistive plate chambers (MRPC), which surrounds the

interaction point and covers the pseudorapidity region $|\eta| < 0.9$ with full-azimuth coverage. The time-of-flight is measured as the difference between the particle arrival time and the event collision time.

The event selection in this study follows those of the previous studies to measure the production of π, K, and p as a function of the charged-particle multiplicity in [3, 27]. The minimum-bias trigger requires signals in both V0A and V0C scintillators in coincidence with the arrival of the proton bunches from both directions. The primary vertex position is reconstructed using global tracks (reconstructed using ITS and TPC information). For events with too few tracks to compute the vertex position, the primary vertex from SPD tracklets (reconstructed using only SPD information) is used instead. Events are required to have a vertex position along the z-axis (parallel to be beam axis) in $|z| < 10$ cm, where $z = 0$ corresponds to the centre of the detector. Events with more than one reconstructed vertex are tagged as pileup events and are discarded. Finally, events are required to have a leading particle. The total number of events after event and vertex selections amounts to about 827 million, while the number of analysed events with a leading particle is about 8.1 million.

The distributions presented in this study correspond to primary charged particles, which are defined as particles with a mean proper lifetime τ larger than 1 cm$/c$, which are either produced directly in the interaction or from decays of particles with τ smaller than 1 cm$/c$, excluding particles produced in interactions with material [28]. Primary charged particles are reconstructed using the ITS and TPC detectors, which provide measurements of the track transverse momentum and azimuthal angle. In particular, tracks are required to cross at least 70 TPC pad rows. They are also required to have at least two hits in the ITS, out of which at least one is in the SPD layers. The fit quality for the ITS and TPC track points must satisfy $\chi^2_{\mathrm{ITS}}/N_{\mathrm{hits}} < 36$ and $\chi^2_{\mathrm{TPC}}/N_{\mathrm{clusters}} < 4$, respectively, where N_{hits} and N_{clusters} are the number of hits in the ITS and the number of clusters in the TPC associated to the track, respectively. Finally, tracks are also required to have a transverse momentum larger than 0.15 GeV$/c$ and to be reconstructed in $|\eta| < 0.8$. To limit the contamination from secondary particles, a selection on the distance of closest approach (DCA) to the reconstructed vertex in the direction parallel to the beam axis (z) of $|\mathrm{DCA}_z| < 2$ cm is applied. Also, a p_{T}-dependent selection on the DCA in the transverse plane (DCA_{xy}) of the selected tracks to the primary vertex is applied. Moreover, tracks associated with the decay products of weakly decaying kaons ("kinks") are rejected. In ALICE, the set of tracks reconstructed with the above-mentioned selection criteria is commonly referred to as "global tracks".

The use of global tracks yields a significantly non-uniform efficiency as a function of the azimuthal angle and pseudorapidity. In order to obtain a high and uniform tracking efficiency together with good momentum resolution, "hybrid tracks" are used [29, 30]. Hybrid tracks correspond to the union of two different sets of tracks selected with complementary criteria: (i) tracks containing at least one space-point reconstructed in one of the two innermost layers of the ITS (global tracks) and (ii) tracks without an associated hit in the SPD for which the position of the reconstructed primary vertex is used in the fit of the tracks. Hybrid tracks are used to select the leading particle, as well as to measure N_{T} and the p_{T} spectra. Furthermore, in order to select high-quality high-p_{T} tracks, a selection based on the geometrical track length (L) is applied [31]. This selection criterion excludes the information from the readout pads at the TPC sector boundaries (≈ 3 cm from the sector edges).

2.2 Particle identification

ALICE's tracking and particle identification (PID) capabilities allow measuring the transverse momentum spectra of π, K, and p over a wide range of transverse momentum. In this study the p_{T} spectra are measured in the $p_{\mathrm{T}} < p_{\mathrm{T}}^{\mathrm{leading}}$ interval, using the standard particle identification techniques which have been reported in previous ALICE publications [3, 27, 32–34]. Table 1 shows the three techniques used for the PID and the p_{T} intervals each method covers.

At low p_{T}, the average energy loss, $\langle \mathrm{d}E/\mathrm{d}x \rangle$, is proportional to $1/(\beta\gamma)^2$ and the relatively large $\pi - \mathrm{K}$ and $\mathrm{p} - \mathrm{K}$ separation power makes it possible to perform particle identification in this region on a track-

Table 1: The name of the analysis technique and the transverse momentum ranges in which π, K and p are identified.

Analysis	p_{T} ranges (GeV/c)		
	π	K	p
TPC	$0.25-0.7$	$0.3-0.6$	$0.45-1.0$
TOF	$0.7-3.0$	$0.6-3.0$	$1.0-3.0$
rTPC	$2.0-5.0$	$3.0-5.0$	$3.0-5.0$

by-track basis [27]. Thus in the TPC analysis, the relative particle abundances, which are defined as the measured fractions of π, K, and p with respect to all the measured primary charged particles are obtained from fitting n_σ distributions in narrow intervals of transverse momentum. For each track, the n_σ is defined as the difference between the measured and expected $\mathrm{d}E/\mathrm{d}x$ values normalised to the resolution, $\mathrm{n}_\sigma = (\mathrm{d}E/\mathrm{d}x_{\mathrm{measured}} - \langle \mathrm{d}E/\mathrm{d}x_{\mathrm{expected}} \rangle)/\sigma$. While the signal of π and p can be fitted with a Gaussian parameterisation, the one for K uses the sum of two Gaussians as parameterisation to take into account the contamination by electrons.

In the TOF analysis, the particle abundances are also measured on a track-by-track basis by fitting the measured β[1] distributions in momentum intervals. In the interval $1 < p < 2$ GeV/c, the $\pi-\mathrm{K}$ and $\mathrm{p}-\mathrm{K}$ separation power of hadron identification is large enough [27] such that one can perform single fits to the signal of π, K, and p using a Gaussian parameterisation convoluted with an exponential tail. The parameters (μ, σ and ξ, where μ and σ represent the mean and standard deviation of the Gaussian paramerisation, and ξ represents the β value at which the exponential tail begins) of the single fits are extracted from data in $1 < p < 2$ GeV/c and are used to extrapolate to higher momentum values. Finally, the extrapolated functional forms are used to fit the β distributions with the sum of three contributions to describe the signals of the three species simultaneously.

In the rTPC analysis, the method described in [32–34] is used. In the relativistic rise region of the TPC ($3 \lesssim \beta\gamma \lesssim 1000$), the $\langle \mathrm{d}E/\mathrm{d}x \rangle$ increases as $\log(\beta\gamma)$ and the $\pi-\mathrm{K}$ and $\mathrm{p}-\mathrm{K}$ separation power for hadron identification is almost constant [27]. The knowledge of these two features makes it possible to perform a two-dimensional fit of the correlation between $\mathrm{d}E/\mathrm{d}x$ and momentum. In order to accomplish this, the first step is to parameterise the Bethe-Bloch and resolution curves in the relativistic rise region. The Bethe-Bloch parameterisation provides the relation between the $\langle \mathrm{d}E/\mathrm{d}x \rangle$ and $\beta\gamma$, and the parameterised resolution gives the relation between $\sigma_{\mathrm{d}E/\mathrm{d}x}$ and $\langle \mathrm{d}E/\mathrm{d}x \rangle$. For the parameterisation, high-purity samples of identified hadrons are used, namely $\mathrm{p}(\bar{\mathrm{p}})$ and $\pi^{\pm}$ from $\Lambda(\overline{\Lambda})$ and $\mathrm{K}^0_{\mathrm{S}}$ decays, respectively, and $\mathrm{e}^{\pm}$ from γ-conversions [32–34]. Once the Bethe-Bloch and resolution curves are parameterised, they are used to perform the two-dimensional fit. The two-dimensional fit is only used to improve the Bethe-Bloch parameterisation in the transition to the plateau region. Then, the particle ratios are obtained from one-dimensional fits to the $\mathrm{d}E/\mathrm{d}x$ distributions in momentum intervals using the sum of four Gaussians as a fit function to describe simultaneously the signal of π, K, p, and e, where the μ and σ of each of the Gaussian distributions are fixed based on the $\langle \mathrm{d}E/\mathrm{d}x \rangle(\beta\gamma)$ and $\sigma_{\mathrm{d}E/\mathrm{d}x}(\langle \mathrm{d}E/\mathrm{d}x \rangle)$ obtained with the above procedure.

2.3 Corrections

The p_{T} spectra of π, K, and p are corrected for acceptance and reconstruction inefficiency. The spectra measured with the TOF detector are also corrected for TPC–TOF matching inefficiency. The acceptance and efficiencies are obtained from simulations using the PYTHIA8 Monte Carlo event generator with the Monash 2013 tune [35]. Subsequently, the propagation of simulated particles through the ALICE apparatus is carried out using GEANT3 [36]. The simulated events are reconstructed using the same algorithms as for the data. The obtained acceptance and reconstruction efficiencies are independent of

[1] $\beta = L/c\Delta t$, where L is the track length and Δt is the measured time-of-flight.

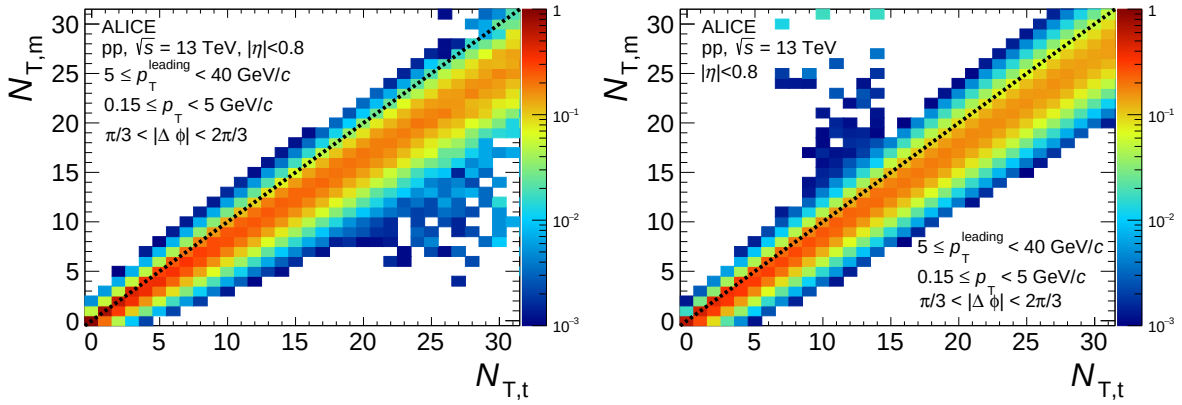

Figure 2: (Left) Correlation between the true $N_{\mathrm{T,t}}$ and the measured $N_{\mathrm{T,m}}$ multiplicity in the transverse region. (Right) Unfolding matrix $\mathrm{M1_{tm}}$. The iteration step of the unfolding matrix corresponds to the third.

the charged-particle multiplicity. Hence, the R_{T}-integrated values are applied for all the R_{T} classes. As GEANT3 does not fully describe the interaction of low-momentum $\overline{\mathrm{p}}$ and K^- with the detector material, an additional correction factor to the efficiency for these two particles is estimated with GEANT4 [37] and FLUKA [38], respectively. These corrections are the same as the ones applied in [3].

The p_{T} spectra of π and p contain a large contribution from secondary particles from interactions in the material and particle decays ($\pi^{\pm}$ from $\mathrm{K^0_S}$ and $\mathrm{p}(\overline{\mathrm{p}})$ from Λ and Σ^+). Since the strangeness production is underestimated in the Monte Carlo event generators, a data-driven approach is used to estimate the fraction of non-primary particles as a function of p_{T} so that it can be subtracted from the measured spectra. The estimation of this correction is based on a multi-template fit to measured DCA_{xy} distributions [39]. In practice, three Monte Carlo templates representing the expected shapes of DCA_{xy} distributions of primary particles, secondaries from weak decays, and secondaries from interactions in the material are used. The fits are performed in $|\mathrm{DCA}_{xy}| \leq 3$ cm. Since the TOF analysis only uses tracks matched with the TOF detector, these corrections are estimated separately for the low- and intermediate-p_{T} regions. At $p_{\mathrm{T}} = 0.45$ GeV/c the contribution from non-primary $\pi^+(\mathrm{p})$ was found to be about $4\%(20\%)$ while at $p_{\mathrm{T}} = 2.0$ GeV/c it decreases to about $1\%(4\%)$. Furthermore the correction decreases asymptotically at higher p_{T}. Therefore, the correction for the TOF is extrapolated to higher p_{T} and then applied.

2.4 Unfolding the charged-particle multiplicity distributions

The charged-particle multiplicity in the transverse region, N_{T}, is used to characterise the event activity. However, the limited acceptance and finite resolution of the detector cause a smearing of the measured charged-particle multiplicity distribution $Y(N_{\mathrm{T,m}})$. This section introduces the one-dimensional unfolding method to correct for these detector effects and efficiency losses. The adopted approach is based on the iterative Bayesian unfolding method by G. D'Agostini [40]. Bayesian unfolding requires the knowledge of the smearing matrix S_{mt}, which comprises information about the limited acceptance and finite resolution. It represents the conditional probability $P(N_{\mathrm{T,m}}|N_{\mathrm{T,t}})$ of an event with the true multiplicity $N_{\mathrm{T,t}}$ to be measured as one with multiplicity $N_{\mathrm{T,m}}$. Figure 2 (left) shows the smearing matrix obtained with simulated events using PYTHIA8 with Monash tune [35]. The values along the diagonal of the smearing matrix represent the probability that a measured event is reconstructed with the true number of particles. At the same time, the off-diagonal elements give the probability that fewer or more particles are reconstructed due to detector inefficiencies and background, e.g., secondary particles misidentified as primary particles.

The one-dimensional unfolded distribution $Y(N_{\mathrm{T,t}})$ is given as the linear combination between the elements of the unfolding matrix $\mathrm{M1_{tm}}$ (see the right panel of Fig. 2) and the measured distribution,

$$Y(N_{\mathrm{T,t}}) = \sum_{\mathrm{m}} \mathrm{M1}_{\mathrm{tm}} Y(N_{\mathrm{T,m}}) \quad \text{, where} \quad \mathrm{M1}_{\mathrm{tm}} = \frac{P(N_{\mathrm{T,m}}|N_{\mathrm{T,t}})\, P_0(N_{\mathrm{T,m}})}{\sum_t P(N_{\mathrm{T,m}}|N_{\mathrm{T,t}})\, P_0(N_{\mathrm{T,m}})} \,. \tag{1}$$

$P_0(N_{\mathrm{T,m}})$ represents a prior probability distribution. It can be any arbitrary distribution at the start of the unfolding process. Here, the measured multiplicity distribution is used as the prior distribution. An updated prior distribution,

$$\widehat{P}(N_{\mathrm{T,t}}) = \frac{Y(N_{\mathrm{T,t}})}{\sum_{N_{\mathrm{T,t}}} Y(N_{\mathrm{T,t}})} \,, \tag{2}$$

is obtained from the second iteration and onwards. Thus, the unfolding matrix is improved as the prior distribution is updated. Finally, a new unfolded distribution closer to the true one can be obtained using Eq. 1 with the updated $\mathrm{M1}_{\mathrm{tm}}$. The smearing in Fig. 2 left shows very few events below the main correlation band between $7 < N_{\mathrm{T,t}} < 15$ and $15 < N_{\mathrm{T,m}} < 30$. This small population comes from statistical fluctuations of the response matrix. Since the unfolding matrix $\mathrm{M1}_{\mathrm{tm}}$ is proportional to $P(N_{\mathrm{T,m}}|N_{\mathrm{T,t}})$, these events show up in $\mathrm{M1}_{\mathrm{tm}}$ in the intervals $22 < N_{\mathrm{T,t}} < 30$ and $7 < N_{\mathrm{T,m}} < 17$, as can be seen in Fig. 2 right. However, given their very small contribution, they are not affecting the unfolding process.

This iterative process makes the unfolded distribution to converge to the true one eventually. However, it also compounds the effects of statistical uncertainties in the smearing matrix. Therefore, a larger number of iterations does not guarantee a better result: eventually, the true distribution might be contaminated by statistical fluctuations [41]. In order to decide when to stop the iterations, the χ^2/N_{df} between the unfolded and the true distribution as a function of the number of iterations is computed for a Monte Carlo generated sample. The minimum value of the ratio χ^2/N_{df} indicates when to stop the iterative process. This study found that the optimal number of iterations is three.

2.5 Unfolding the p_{T} spectra

Unfolding the transverse momentum spectra as a function of the multiplicity is treated differently depending on the topological region. The toward and away regions turned out to be straightforward cases as there is no overlap between the tracks used for the spectra and the tracks used for the multiplicity calculation as the latter is measured in the transverse region. Therefore, the one-dimensional unfolding matrix $\mathrm{M1}_{\mathrm{tm}}$ is directly applied in these two regions. This also makes it trivial to see that the same unfolding matrix can be used for all identified particle spectra. Hence, the fully corrected p_{T} spectra as a function of $N_{\mathrm{T,t}}$ are obtained in a two-step procedure:

1. Correct the raw p_{T} spectra at particle level for tracking inefficiency and secondary particle contamination. The efficiency correction is applied here as the one-dimensional unfolding only affects the classification of the events.

2. Apply the one-dimensional unfolding matrix. The spectra as a function of $N_{\mathrm{T,t}}$ are given by: $\frac{\mathrm{d}Y(N_{\mathrm{T,t}})}{\mathrm{d}p_{\mathrm{T}}} = \sum_{\mathrm{m}} \mathrm{M1}_{\mathrm{tm}} \frac{\mathrm{d}Y(N_{\mathrm{T,m}})}{\mathrm{d}p_{\mathrm{T}}}$

The transverse region requires a more elaborate method since both p_{T} spectra and multiplicity are measured using the same tracks. In other words, one is no longer dealing with the problem of rearranging events but rather how tracks should be unshuffled to match the true transverse momentum distributions. This poses a multi-dimensional problem with two dimensions associated to the true and measured multiplicities and two additional dimensions (true and measured yields) for each p_{T} bin. Instead of performing the full multi-dimensional unfolding, an approximate method is employed in which the multiplicity

smearing matrix is assumed to be independent of the transverse momentum. This is a very good approximation as the efficiency is essentially flat in p_{T} for the track selection and p_{T} ranges used here. In this approach, a new response matrix is obtained by multiplying every column of the original multiplicity response matrix with the respective number of measured particles as weights. After row-wise normalisation, the desired track smearing matrix is obtained.

The unfolding is done bin-by-bin in p_{T} with this modified response matrix. For a particular transverse momentum bin, the measured multiplicity distribution is unfolded using the iterative unfolding procedure described in Sec. 2.4. This approach yields unfolding matrices that depend on the transverse momentum. Henceforth, these matrices will be called $\mathrm{M2}_{\mathrm{tm}}(p_{\mathrm{T}})$. It should be stressed that this method works here because the tracking efficiency does not depend strongly on the transverse momentum for hybrid tracks and because the same tracks to measure N_{T} are used to obtain the spectra.

Similar to the toward and away regions, the two-step procedure is followed to obtain the fully corrected transverse momentum spectra. The only difference is that in the transverse region the p_{T}-dependent $\mathrm{M2}_{\mathrm{tm}}(p_{\mathrm{T}})$ matrices are used

$$\frac{\mathrm{d}Y(N_{\mathrm{T,t}}, p_{\mathrm{T}})}{\mathrm{d}p_{\mathrm{T}}} = \sum_{\mathrm{m}} \mathrm{M2}_{\mathrm{tm}}(p_{\mathrm{T}}) \frac{\mathrm{d}Y(N_{\mathrm{T,m}}, p_{\mathrm{T}})}{\mathrm{d}p_{\mathrm{T}}}. \tag{3}$$

The method described above unfolds the spectra of all charged particles and yields the unfolding matrices $\mathrm{M1}_{\mathrm{tm}}$ and $\mathrm{M2}_{\mathrm{tm}}(p_{\mathrm{T}})$. When unfolding the spectra of identified particles (for example, π in the transverse region), Eq. 3 is applied using the $\mathrm{M2}_{\mathrm{tm}}(p_{\mathrm{T}})$ matrices from charged particles and then exchanging $\mathrm{d}Y(N_{\mathrm{T,m}}, p_{\mathrm{T}})/\mathrm{d}p_{\mathrm{T}}$ for $\mathrm{d}Y^{\pi}(N_{\mathrm{T,m}}, p_{\mathrm{T}})/\mathrm{d}p_{\mathrm{T}}$. The unfolding of π spectra in the toward and away regions is done with the same strategy but using $\mathrm{M1}_{\mathrm{tm}}$ instead.

3 Systematic uncertainties

In this section, the estimation of the systematic uncertainties is described. The systematic uncertainties on the p_{T} spectra are divided into two categories, R_{T}-dependent and R_{T}-independent uncertainties. The total systematic uncertainty on the p_{T} spectra is given as the sum in quadrature of all the individual sources of uncertainty.

R_{T}-dependent systematic uncertainties

The unfolding method described in Sec. 2.4 shows deficiencies, mainly when unfolding the p_{T} spectra for low multiplicities in the transverse region. To account for these deficiencies, the following contributions to the systematic uncertainty on the N_{T} distribution are considered:

- Monte Carlo (MC) non-closure: PYTHIA8 with Monash tune is the default model used to generate the multiplicity response matrix and N_{T} distributions with and without the detector's efficiency losses. The unfolded N_{T} spectrum from the simulation is compared to the generated one. Thus, any statistically significant difference between the generated and unfolded distributions is referred to as MC non-closure and is added in quadrature to the total systematic uncertainty. During the unfolding procedure, the MC closure improves with the number of iterations, with an optimal number of three, which leads to a negligible MC non-closure.

- Dependence on the choice of the MC model: EPOS LHC [42] is used as the alternative model to generate a different multiplicity response matrix. This response matrix is used to unfold the N_{T} and p_{T} spectra. The ratio between the final unfolded distributions using PYTHIA8 and EPOS LHC was quantified and added to the total systematic uncertainty. In the interval $0 < N_{\mathrm{T}} < 18$, the relative systematic uncertainty is below 2 %, increasing to about 4 % at $N_{\mathrm{T}} \approx 18$. Due to statistical

limitations on the response matrix, a constant 4 % relative systematic uncertainty for $N_{\mathrm{T}} \geq 18$ was assigned.

– Track selection: This uncertainty is quantified by changing the track selection criteria with respect to the nominal one. In particular, the minimum number of crossed rows in the TPC is set to 60 and 100 (the nominal is 70). The track fit quality in the ITS and TPC quantified by the $\chi^2_{\mathrm{ITS}}/N_{\mathrm{hits}}$ and the $\chi^2_{\mathrm{TPC}}/N_{\mathrm{clusters}}$ must not exceed 25 and 49 (the nominal is 36), and 3 and 5 (the nominal is 4), respectively. The maximum distance of closest approach to the vertex along the beam axis (DCA_z) is set to 1 and 5 cm (the nominal is 2 cm). Furthermore, the parameters of the geometrical length cut to select the leading particle are also varied. For a particular parameter variation, the maximum difference between the results obtained with the tighter and looser selections with respect to the nominal value is quantified. The total systematic uncertainty from track variations is given as the sum in quadrature of the different parameter variations. The relative systematic uncertainty is on average 1 % in the interval $0 < N_{\mathrm{T}} < 18$ and increases for higher N_{T} values. For $N_{\mathrm{T}} \geq 18$, the statistical fluctuations become significant. Therefore, a constant 2 % relative systematic uncertainty was assigned.

R_{T}-independent systematic uncertainties

The R_{T}-independent systematic uncertainties are divided into two categories. The first category includes the uncertainties common to the different analyses, such as those due to the track quality criteria and the p_{T}-dependent ITS–TPC matching efficiency. The second category groups the analysis specific uncertainties. It includes the uncertainties on the secondary particle contamination correction estimation, the signal extraction technique and the TPC–TOF matching efficiency.

As described in Sec. 2.3, the secondary particle contamination correction is based on multi-template fits to the DCA_{xy} distributions in transverse momentum intervals. The estimation of the systematic uncertainty follows the procedure described in [27]. Namely, the fitting range is changed from the nominal values of ± 3 cm to ± 1.5 cm.

To estimate possible systematic effects attributed to the signal extraction technique in the TPC analysis, a similar procedure to the one described in [27] was applied. The signal extraction technique changed from fitting n_σ distributions to bin counting in the range of $\pm 3\sigma$. The systematic uncertainty on the particle fractions is given as the difference between the nominal particle fractions and the ones obtained from bin counting.

As described in Sec 2.2, the measurement of the particle fractions in the TOF analysis is based on fits to β distributions in momentum intervals. Hence, the systematic uncertainty is mainly driven by the uncertainty in the parameterisation of the μ, σ, and ξ curves for π, K, and p. The relative difference between the fitted curves and the actual measured μ, σ, and ξ values was computed to evaluate the effect of the parameterisations. Thus, the systematic uncertainty in the extraction of the particle fractions is obtained by refitting the β distributions while randomly varying the constrained parameters μ, σ, and ξ within the uncertainty of the parameterisations assuming a Gaussian variation centred at the nominal value. The refitting was performed 1000 times, and the systematic uncertainty on the particle fractions as a function of the transverse momentum is given as the standard deviation of the associated distributions. This approach is motivated by work developed in [27, 32, 34].

The measurement of the systematic uncertainty on the extraction of the particle fractions in the rTPC analysis follows the method from [27, 32, 34]. In this analysis, the primary source of systematic uncertainty comes from the imprecise description of the detector response, namely the Bethe-Bloch and resolution parameterisations. To estimate the systematic effect, the relative difference between the parameterisations and the actual $\langle \mathrm{d}E/\mathrm{d}x \rangle$ and $\sigma_{\mathrm{d}E/\mathrm{d}x}$ values are measured. The particle fractions are measured following a fitting procedure where the constrained parameters, $\langle \mathrm{d}E/\mathrm{d}x \rangle$ and $\sigma_{\mathrm{d}E/\mathrm{d}x}$, are allowed

to vary randomly within the uncertainty of the parameterisations. The fitting procedure was repeated 1000 times and the systematic uncertainty in the particle fractions is given as the standard deviation of the associated distributions.

When computing the p_{T}-differential particle ratios, all the systematic uncertainties cancel out in the ratios except those attributed to the signal extraction and feed-down. In the high p_{T} region (rTPC analysis) the procedure described in [32] is used to extract the signal extraction systematic uncertainty on the K/π and p/π ratios directly from fits to the $\mathrm{d}E/\mathrm{d}x$ distributions.

Table 2 lists a summary of the systematic uncertainties at different p_{T} values for the spectra and particle ratios in the transverse region. The table is divided into common and analysis-specific uncertainties. The values in the toward and away regions are the same as those of the transverse region. The only topological-region-dependent uncertainty is the one attributed to the MC non-closure.

Table 2: Summary of systematic uncertainties on the π, K, and p p_{T} spectra. The uncertainties are shown for different representative p_{T} values. The last two rows show the total systematic uncertainty on the p_{T} spectra and the p_{T}-differential particle ratios. These values correspond to the spectra in the transverse region in the $0 \leq R_{\mathrm{T}} < 0.5$ class.

	Uncertainty (%)								
Common source		π			K			p	
p_{T} (GeV/c)	0.3	2	5	0.3	2	5	0.45	2	5
ITS–TPC matching efficiency	1.4	2.6	2.9	1.4	2.6	2.9	1.4	2.6	2.9
MC non-closure		3.2			3.6			1.5	
MC dependence	1	1.5	1.7	0.9	1.5	1.7	0.9	1.5	2
Track selection		1			1			1	
Analysis-specific		π			K			p	
TPC, p_{T} (GeV/c)	0.3		0.7	0.3		0.6	0.45		1
PID	0.1		1.8	7.3		5.9	0.1		3.4
Feed-Down	1		0.3	-		-	10		1.1
TOF, p_{T} (GeV/c)	1		2	1		2	1		2
PID	negl.		1	0.3		3.4	0.2		0.7
Feed-Down	0.3		negl.	-		-	1		0.2
TOF matching efficiency	3		3	6		6	4		4
rTPC, p_{T} (GeV/c)	3		5	3		5	3		5
PID	0.7		0.6	6.4		2.8	5.8		4.2
Feed-Down	negl.		negl.	-		-	0.2		0.2
Total		π			K			p	
p_{T} (GeV/c)	0.3	2	5	0.3	2	5	0.45	2	5
Total	3.9	5.5	4.7	8.3	8.3	5.7	10.2	5.3	5.7
Particle ratios					K/π			p/π	
p_{T} (GeV/c)				0.3	2	5	0.45	2	5
Total				7.4	4.1	3.2	10.1	1.5	4

4 Results

This section presents the results of the production of π, K, and p as a function of the relative transverse activity classifier, R_{T}. The data are compared with model predictions from PYTHIA8 with Monash 2013 tune (indicated as PYTHIA8 Monash in the following) [35], PYTHIA8 with ropes hadronisation model (indicated as PYTHIA8 ropes) [43], Herwig [12, 13], and EPOS LHC [42]. PYTHIA8 Monash is one of the most popular event generators at LHC energies for most observables but lacks the QGP-like effects observed in small collision systems such as strangeness enhancement, while the other three models are known to describe the strangeness enhancement in small collision systems better [8, 43, 44]. Hence, these models allow for testing a broad range of possible dynamic effects. In PYTHIA8 Monash, the soft-inclusive particle production is based on multiple perturbative parton–parton interactions (MPI) [45]. This model also includes a colour reconnection (CR) mechanism [46], allowing each MPI system's partons to be colour connected with a higher-p_{T} MPI system. In particular, PYTHIA describes the enhanced p_{T}-differential proton-to-pion ratio at intermediate p_{T} by introducing the colour reconnection mechanism and does not need to assume the formation of a medium [47]. PYTHIA8 ropes model allows strings to fuse in an environment with a high density of strings and form "colour ropes". Consequently, colour ropes are expected to produce more strange hadrons and baryons, the latter via probabilistic collapses of ropes to string junctions. EPOS LHC is a core-corona model, which assumes the formation of a QGP medium in the high-density core regions in pp collisions. The hadronisation of the corona is based on string fragmentation, while the particles associated with the core are thermally produced (grand-canonical thermal description). In EPOS LHC, particle production in low-multiplicity events is mainly dominated by string fragmentation. In contrast, high-multiplicity events are core dominated, and a large production of strange hadrons and baryons is expected. Particle production in the Herwig model is based on cluster hadronisation and it has its own colour reconnection mechanism where baryonic clusters are allowed to be produced in a geometric manner. This model also includes a non-perturbative gluon splitting mechanism to create more $\mathrm{s\bar{s}}$ pairs to account for the strangeness enhancement [48].

The p_{T} spectra as a function of R_{T} are normalised to the total number of events in each R_{T} class. The relation between R_{T} intervals and N_{T} classes is given in Table 3. The R_{T} distribution is constructed using the unfolded N_{T} distribution for which the $\langle N_{\mathrm{T}} \rangle$ is equal to 7.366 ± 0.002 (stat.).

Table 3: Relation between R_{T} intervals and N_{T} classes.

$R_{\mathrm{T}} = N_{\mathrm{T}}/\langle N_{\mathrm{T}} \rangle$	N_{T}	Number of events
0–0.5	0–3	2613151
0.5–1.5	4–11	4055410
1.5–2.5	12–18	1302116
2.5–5	19–30	180652
0–5	0–30	8151331

Figure 3 shows the unfolded N_{T} and R_{T} probability distributions in the transverse region integrated over all the events with the leading particle along with different model predictions. For each model, the $\langle N_{\mathrm{T}} \rangle$ corresponds to the mean value of the corresponding N_{T} spectrum. It is observed that PYTHIA8 Monash and PYTHIA8 ropes give the best qualitative description of the N_{T} distribution, while EPOS LHC (Herwig) overestimates (underestimates) the data for $N_{\mathrm{T}} > 10$. However, when R_{T} is computed, all the models underestimate the data for $R_{\mathrm{T}} \gtrsim 2$. This is because the models poorly describe the low-N_{T} region, so they predict larger $\langle N_{\mathrm{T}} \rangle$ values than the measured ones. Finally, the R_{T} probability distribution is compared with the previous ALICE result [16], which used a limited data sample and applied the unfolding at the level of the R_{T} distribution while in the current analysis the R_{T} spectrum is derived from the N_{T} distribution. The new result is in agreement with the previous ALICE measurement within 1.5%.

Figures 4 to 6 show the transverse momentum distributions of π, K, and p as a function of R_{T}. The results in the toward, away, and transverse regions are shown on the left, middle, and right panels, re-

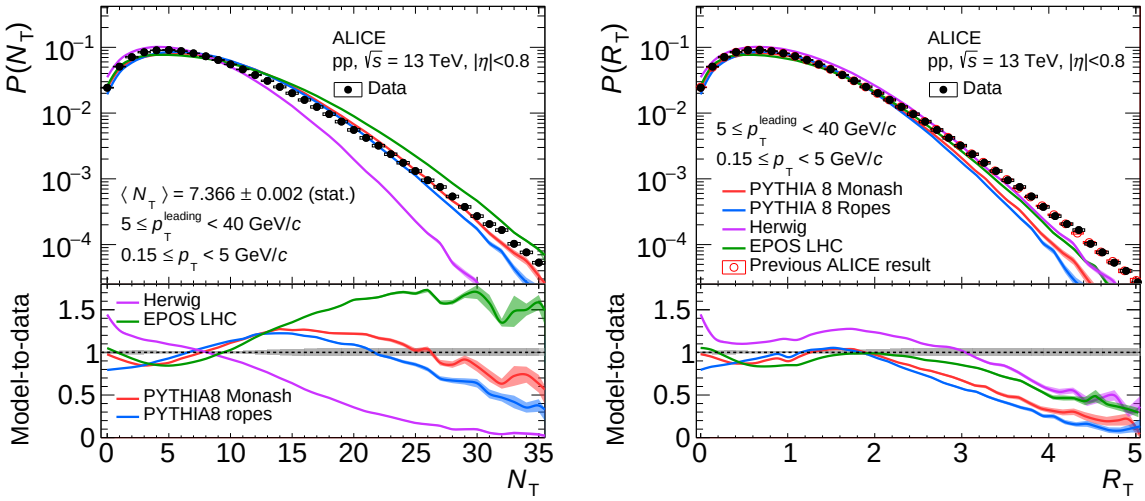

Figure 3: N_{T} (left) and R_{T} (right) probability distributions in the transverse region in events with the leading particle. The data are represented with solid black markers and statistical and systematic uncertainties with error bars and boxes, respectively. Model predictions are presented with colour lines and the bands around the model predictions represent only the statistical uncertainty. The bottom panels show the model-to-data ratios. The grey band centred at one in the bottom panel represents the systematic uncertainties of the data.

spectively. The lower panels show the ratios between the R_{T}-dependent p_{T} spectra and the R_{T}-integrated p_{T} spectrum. The R_{T}-independent systematic uncertainties cancel out in the ratios. The R_{T}-dependent systematic uncertainties are correlated and cancel out only partly. From the ratios to the R_{T}-integrated spectrum, it is observed that the toward and away regions share a similar feature at low transverse momentum: a depletion of low-p_{T} particles with increasing R_{T}. Furthermore, this effect follows a mass ordering, being larger for heavier particles. This behaviour is reminiscent of radial flow effects, in which the depletion of low-p_{T} particles is compensated by an increasing number of particles at intermediate p_{T}. The particle production in the toward and away regions is dominated by the leading and away-side jet fragmentation into high-p_{T} particles. This can be observed in the ratio between the spectra in $0 \leq R_{\mathrm{T}} < 0.5$ and the R_{T}-integrated ones (bottom panels of Figures 4 to 6), which increases with p_{T} (in the interval $p_{\mathrm{T}} \gtrsim 2$ GeV/c), and the effect is more evident for pions. The opposite is observed for the spectral shapes at high R_{T}; they soften with increasing R_{T} for $p_{\mathrm{T}} \gtrsim 2$ GeV/c. This can be interpreted as a "dilution" of the jet with increasing UE activity. The jet is always part of the event, irrespective of R_{T}, however, at large R_{T}, the toward and away regions are dominated by the UE. The spectral shapes of all the species in the transverse region share a common feature: they harden with increasing UE activity. This effect can be attributed to jet hardening with increasing multiplicity.

Figure 7 shows model-to-data ratios for the p_{T} spectra. The ratios are shown for two R_{T} intervals: $0 \leq R_{\mathrm{T}} < 0.5$ and $2.5 \leq R_{\mathrm{T}} < 5$. It is observed that the models can describe the pion and kaon spectra for $p_{\mathrm{T}} > 2$ GeV/c in the toward and away regions qualitatively when the UE is suppressed $(0 \leq R_{\mathrm{T}} < 0.5)$. This is expected since for small R_{T} values, one mainly observes the jet fragmentation products, and the models are tuned to $\mathrm{e^+e^-}$ data, which are jet-like. For this same R_{T} interval, one can see that all the models underestimate the soft particle production. Moreover, increasing the UE activity $(2.5 < R_{\mathrm{T}} < 5)$ makes the agreement between data and models worse.

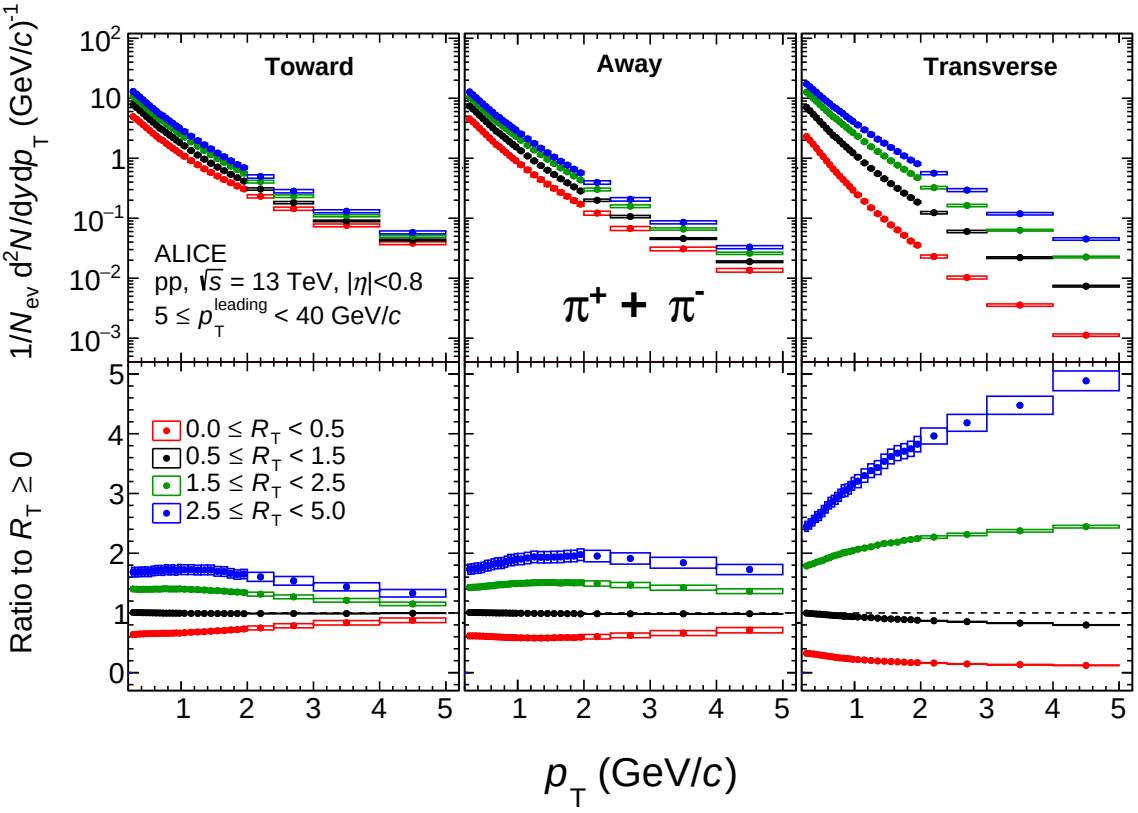

Figure 4: Transverse momentum spectra (top panels) of pions as a function of R_{T} and ratios to the R_{T}-integrated spectrum (bottom panels). The toward, away, and transverse regions are shown from left to right. The statistical and systematic uncertainties are represented with bars and boxes, respectively.

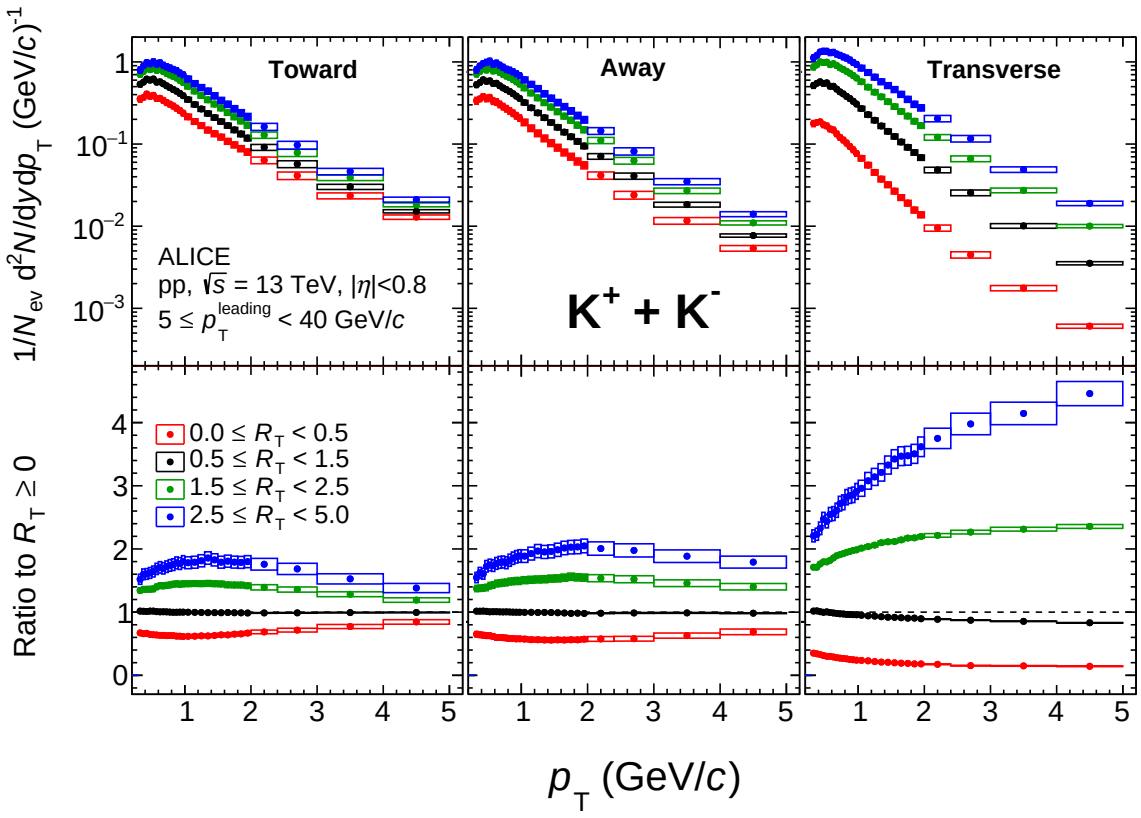

Figure 5: Transverse momentum spectra (top panels) of kaons as a function of R_{T} and ratios to the R_{T}-integrated spectrum (bottom panels). The toward, away, and transverse regions are shown from left to right. The statistical and systematic uncertainties are represented with bars and boxes, respectively.

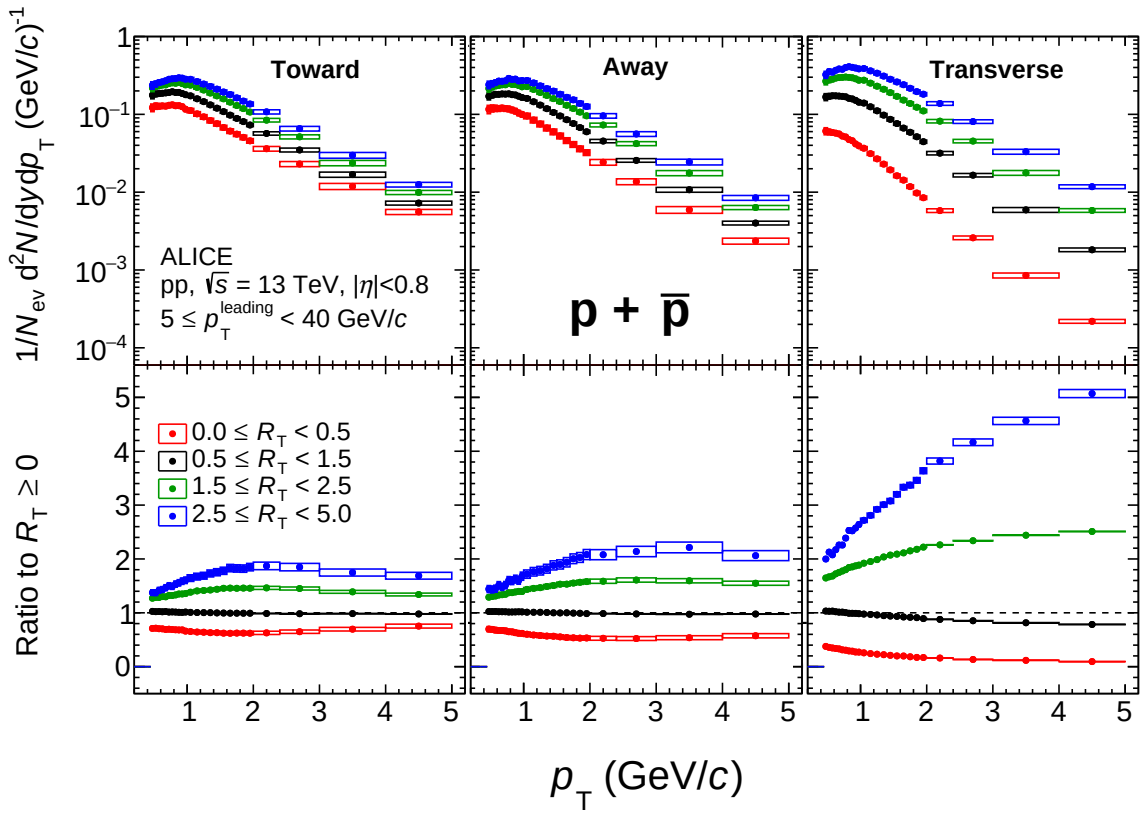

Figure 6: Transverse momentum spectra (top panels) of protons as a function of R_{T} and ratios to the R_{T}-integrated spectrum (bottom panels). The toward, away, and transverse regions are shown from left to right. The statistical and systematic uncertainties are represented with bars and boxes, respectively.

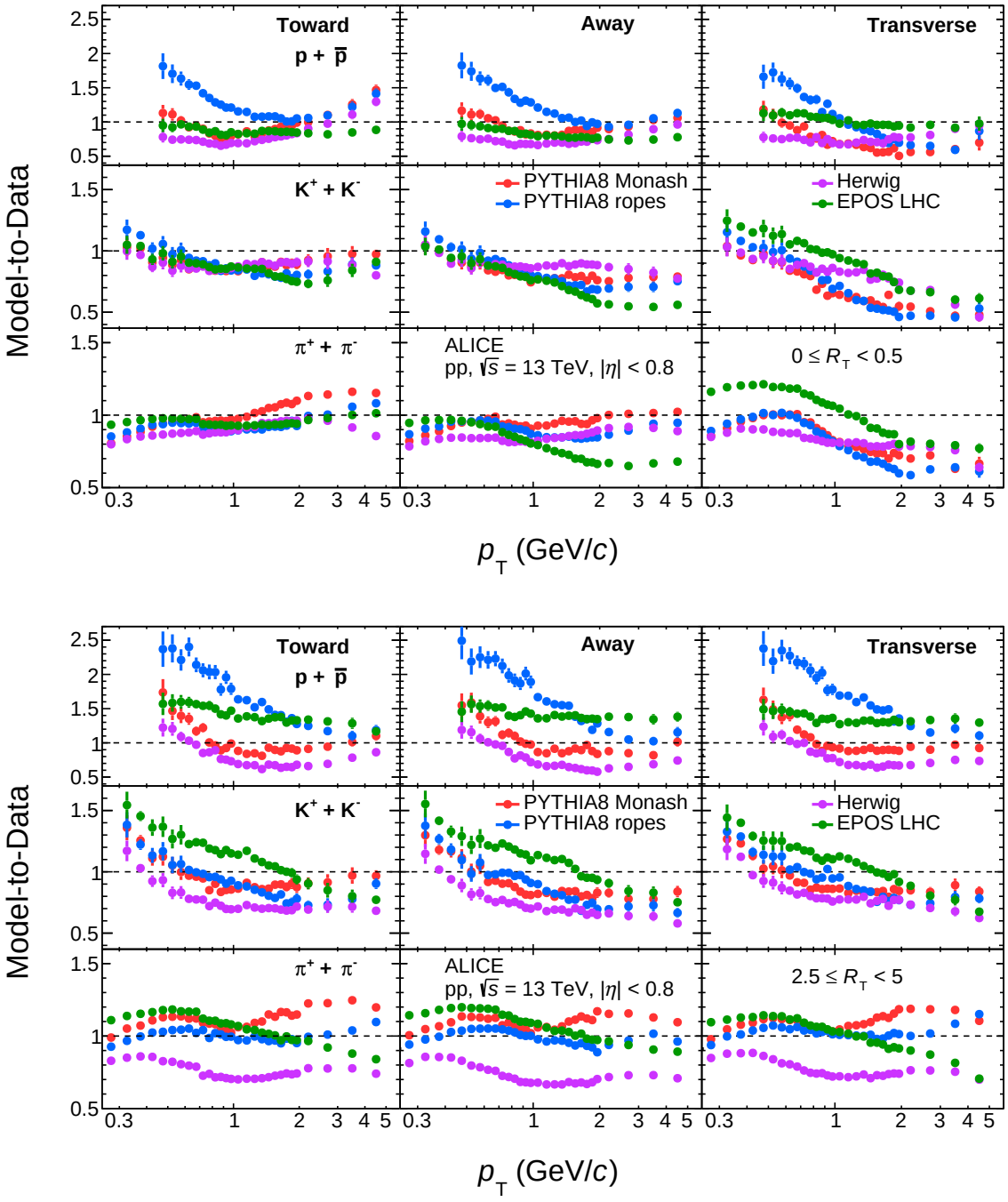

Figure 7: Model-to-data ratios of the transverse momentum spectra. The results are shown for two R_{T} intervals: $0 \leq R_{\mathrm{T}} < 0.5$ (top figure) and $2.5 \leq R_{\mathrm{T}} < 5$ (bottom figure). The ratios in the toward, away and transverse regions are shown on the left, middle and right column, respectively. The error bars represent the combination of the statistical and systematic uncertainties on the model-to-data ratios.

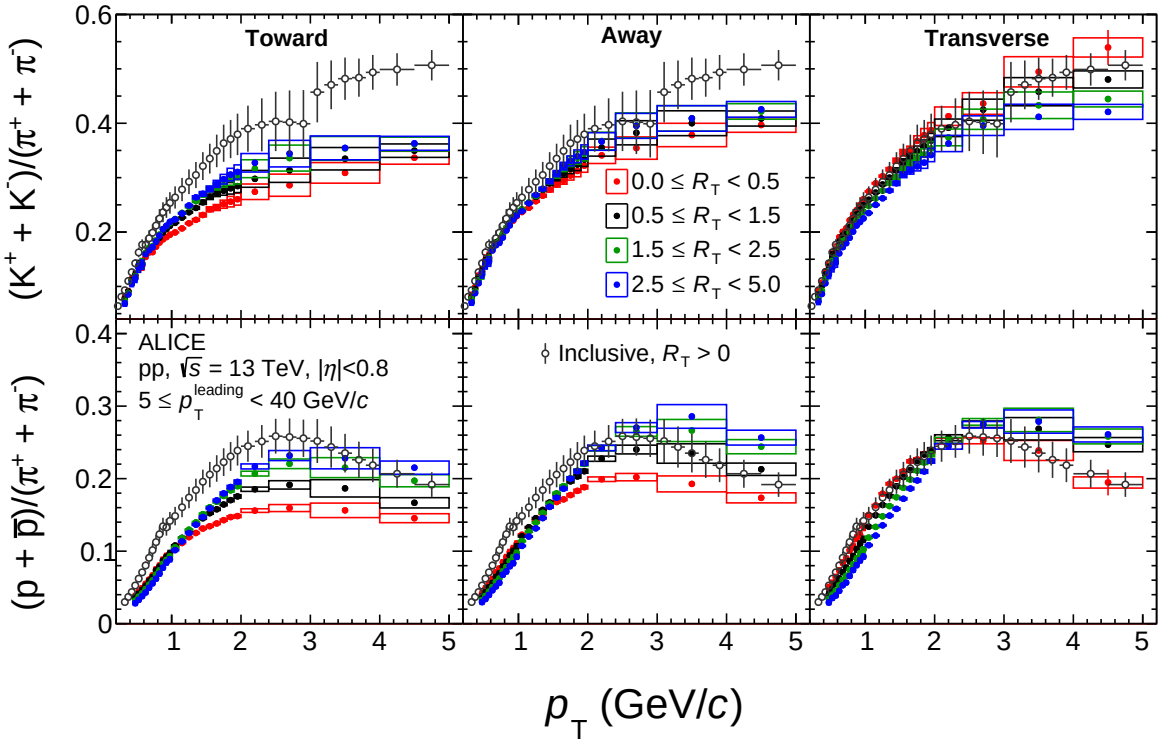

Figure 8: p_{T}-differential particle ratios as a function of R_{T}. The top (bottom) row shows the K/π (p/π) ratio. The results in the toward, away, and transverse regions are shown from left to right. Statistical and systematic uncertainties are represented with error bars and boxes, respectively. The inclusive minimum-bias particle ratios in pp collisions at the same centre-of-mass energy [3] are overlaid.

Figure 8 shows the p_{T}-differential kaon-to-pion (K/π) and proton-to-pion (p/π) ratios for the four different R_{T} intervals in the three topological regions. The R_{T}-dependent ratios are contrasted with the inclusive ratios in minimum bias collisions at the same centre-of-mass energy [3]. Minimum bias means integrated over R_{T} and the azimuthal angle, and without the leading particle requirement. The K/π ratios in the toward and away regions show similar features: they increase with increasing UE activity. However, this is true only for $1 \lesssim p_{\mathrm{T}} < 2$ GeV/c. Conversely, the K/π ratio in the transverse region decreases with increasing R_{T}. One also observes that the minimum-bias result is very similar to those measured in the transverse region. This suggests that the inclusive K/π ratio is dominated by bulk particle production. The p/π ratio in the toward and away regions measured in the lowest R_{T} intervals is always below the inclusive one. Similar observations have been made for the $\Lambda/\mathrm{K}^0_{\mathrm{S}}$ ratio in jets [49]. As the UE increases, the toward and away regions become more UE dominated (jet dilution) and the p/π ratio also increases. However, this is true only for $p_{\mathrm{T}} \gtrsim 1$ GeV/c. The growth of the p/π ratio might be attributed to a gradual increase of the collective radial flow with R_{T}. Furthermore, the baryon-to-meson ratio for $p_{\mathrm{T}} > 1$ GeV/c in these two regions tends to increase with increasing R_{T} and to approach the minimum bias ratio, which is similar to the one measured in the transverse region. The p/π ratio in the transverse region shows a mild dependence on R_{T}. It is observed that the result in the highest UE activity interval is below the one in the lowest UE activity interval for $p_{\mathrm{T}} \lesssim 2$ GeV/c, indicating a suppression of low-p_{T} protons possibly due to collective radial flow. Furthermore, the observed maximum in the highest R_{T} interval (centred at $p_{\mathrm{T}} \approx 3.5$ GeV/c) is shifted to the right with respect to the one of the lowest R_{T} interval (centred at $p_{\mathrm{T}} \approx 2.5$ GeV/c). This might be attributed to the jet hardening effect with increasing multiplicity as discussed in [14].

Figure 9 shows the p_{T}-differential K/π and p/π ratios along with model predictions in two R_{T} inter-

vals: $0 \leq R_{\rm T} < 0.5$ (low-UE activity) and $2.5 < R_{\rm T} < 5$ (high-UE activity). The K/π and p/π ratios in the toward and away regions in events at low $R_{\rm T}$ can be described qualitatively by PYTHIA8 Monash. However, this model predicts almost no evolution with $R_{\rm T}$. On the other hand, the PYTHIA8 ropes hadronisation model, which allows for the formation of colour ropes, predicts p/π ratios that evolve with $R_{\rm T}$, but overestimates the data, particularly for high-$R_{\rm T}$ events. EPOS LHC also describes both ratios qualitatively in the limit of low UE activity and predicts an evolution with $R_{\rm T}$. It describes the K/π ratio but overestimates the p/π ratio in events with high $R_{\rm T}$. This was clear from the $p_{\rm T}$-integrated particle ratios: the transition from string fragmentation to statistical hadronisation needs improvement. Finally, Herwig also predicts an evolution with $R_{\rm T}$ and can describe rather well the K/π ratio, while it misses the $p_{\rm T}$ trend of the p/π ratio. The fact that all models do a better job at describing both ratios at low than at high $R_{\rm T}$ is expected since they are tuned to $\rm e^+e^-$ data. The model predictions in the away region are similar to those of the toward.

In the transverse region, PYTHIA8 Monash and PYTHIA8 ropes describe the splitting and ordering of the K/π ratio between the two $R_{\rm T}$ classes qualitatively but underestimate the data. They can also describe the p/π ratio qualitatively. Moreover, those models predict the lower p/π ratio for $p_{\rm T} \lesssim 2$ GeV/c in events with high $R_{\rm T}$ compared to the low UE activity ratios. This effect, which can be attributed to the radial flow effects, is likely induced by the CR and ropes in PYTHIA8. EPOS LHC predicts the same K/π ratio for both $R_{\rm T}$ classes, while the p/π ratio at low $R_{\rm T}$ agrees with the data. Still, as previously mentioned, the transition from core-corona hadronisation is not well modeled. Finally, Herwig gives a good qualitative description of the evolution of the p/π ratio with $R_{\rm T}$ in the transverse region.

The $p_{\rm T}$-integrated yield (dN/dy) and the average transverse momentum ($\langle p_{\rm T} \rangle$) of pions, kaons, and protons are extracted from the $p_{\rm T}$-differential spectra in the different $R_{\rm T}$ intervals and topological regions. Since the spectra are measured for $p_{\rm T} > 0.3$ GeV/c (π, K) and $p_{\rm T} > 0.45$ (p) GeV/c, they are first extrapolated to $p_{\rm T} = 0$. The extrapolation procedure is carried out by fitting the spectra with Lévy-Tsallis parameterisations [50, 51]. The parameterisation is only used in the $p_{\rm T}$ intervals with no data. For example, for the $0 \leq R_{\rm T} < 0.5$ interval in the transverse region the fractions of extrapolated yields amount to 38%, 19%, and 22% for π, K, and p, respectively. To estimate the systematic uncertainty associated with the extrapolation procedure, several other parameterisations such as the Fermi-Dirac, Bose-Einstein, Blast-Wave, and $m_{\rm T}$-exponential are used to estimate the extrapolated yield. The maximum difference between the nominal and extrapolated yields is associated as the systematic uncertainty of the extrapolation procedure. For example, the systematic uncertainties on the dN/dy ($\langle p_{\rm T} \rangle$) amount to 2%(1.7%), 2.7%(2.3%), and 2%(1.5%) for π, K, and p, respectively, for the $0 \leq R_{\rm T} < 0.5$ interval in the transverse region.

Figure 10 shows the average transverse momentum as a function of $R_{\rm T}$ in the different topological regions. The $\langle p_{\rm T} \rangle$ of π and K in the toward region is the largest in the $0 \leq R_{\rm T} < 0.5$ (low UE activity) interval. This feature reflects the presence of the jet fragmenting mainly into low-mass hadrons (π and K) with large transverse momentum. As the UE activity increases, the $\langle p_{\rm T} \rangle$ of π and K slowly decreases and tends to flatten for $R_{\rm T} > 1.5$ due to the jet dilution effect: the toward and away regions become dominated by the UE. Conversely, the $\langle p_{\rm T} \rangle$ of protons increases with $R_{\rm T}$, which can be attributed to the additional radial flow effect. Moreover, the $\langle p_{\rm T} \rangle$ of all the species at high-$R_{\rm T}$ tend to approach the values measured at high $R_{\rm T}$ in the transverse region. All models can describe the $\langle p_{\rm T} \rangle$ qualitatively in the toward region, but EPOS LHC is the only one that predicts an increasing trend of the proton $\langle p_{\rm T} \rangle$. Particle production in the away region is similar to that in the toward. It is primarily dominated by the away-side jet. It is observed that the $\langle p_{\rm T} \rangle$ of all the species increases with $R_{\rm T}$. Furthermore, the $\langle p_{\rm T} \rangle$ tends to approach the values of the transverse region at large $R_{\rm T}$ where the UE dominates. PYTHIA8 Monash and ropes give a fair qualitative description of the evolution of $\langle p_{\rm T} \rangle$ of pions with $R_{\rm T}$ in the away region while the $\langle p_{\rm T} \rangle$ of protons in the same region is only described by EPOS LHC.

The $\langle p_{\rm T} \rangle$ in the transverse region increases with $R_{\rm T}$ for all the species; however, the rate of increase

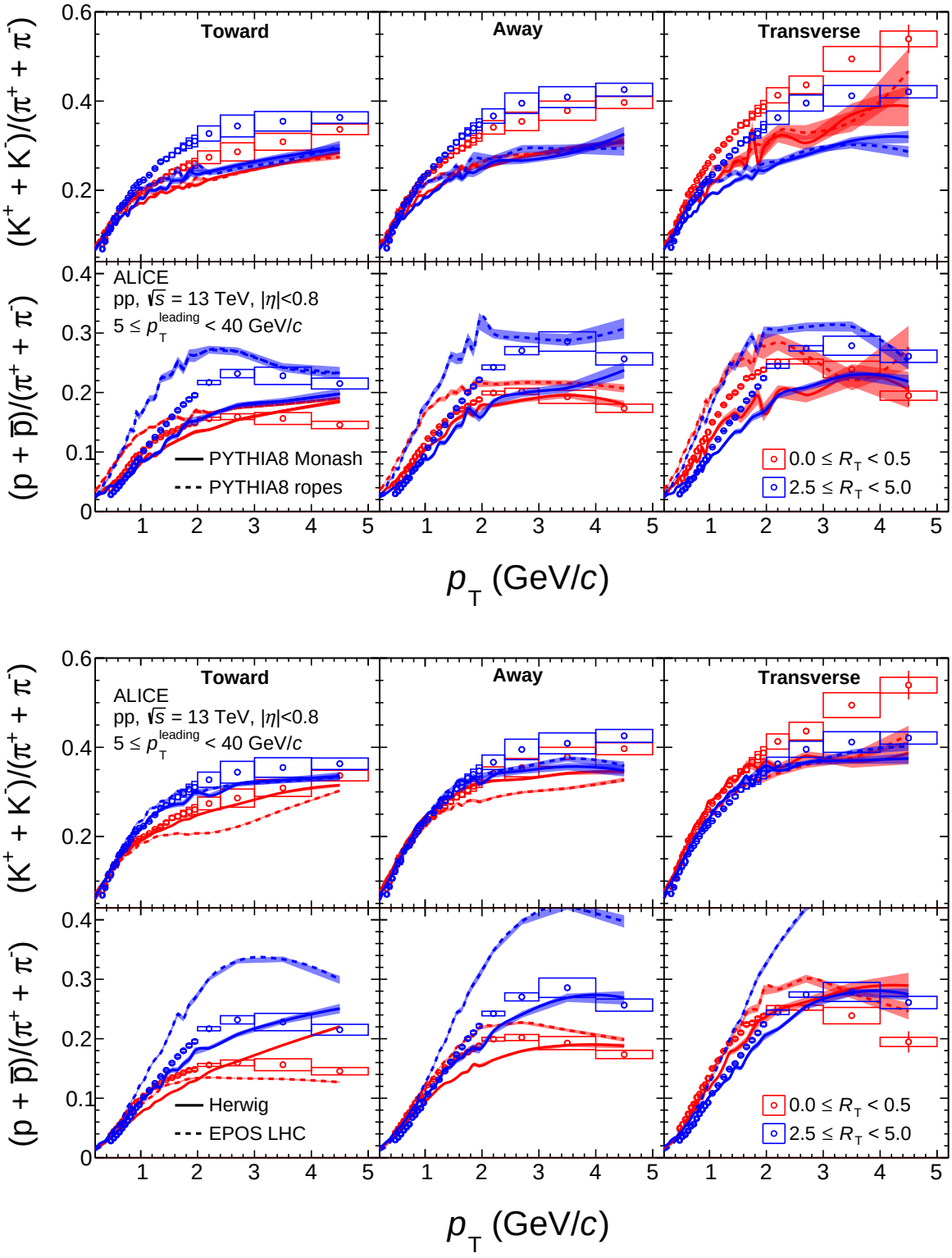

Figure 9: Kaon-to-pion and proton-to-pion ratios as a function of p_{T} for two R_{T} intervals: $0 \le R_{\mathrm{T}} < 0.5$ (red markers) and $2.5 \le R_{\mathrm{T}} < 5$ (blue markers). The particle ratios in the toward, away and, transverse regions are shown from left to right. The PYTHIA 8 Monash and PYTHIA 8 ropes (EPOS LHC and Herwig) predictions are shown in the top (bottom) figure. The shaded regions around the model line represent the statistical uncertainties.

exhibits a mass ordering, being more significant for heavier particles. Similar observations have been made in multiplicity-dependent studies [2, 3]. The rise of the $\langle p_{\mathrm{T}} \rangle$ with increasing R_{T} is likely attributed to autocorrelation effects. Since R_{T} and the p_{T} spectra are measured in the same $\Delta\varphi$ region, the high multiplicity requirement in the transverse region increases the probability to have a jet in the same region. Finally, it is observed that all the models predict the increase of the $\langle p_{\mathrm{T}} \rangle$ with R_{T}.

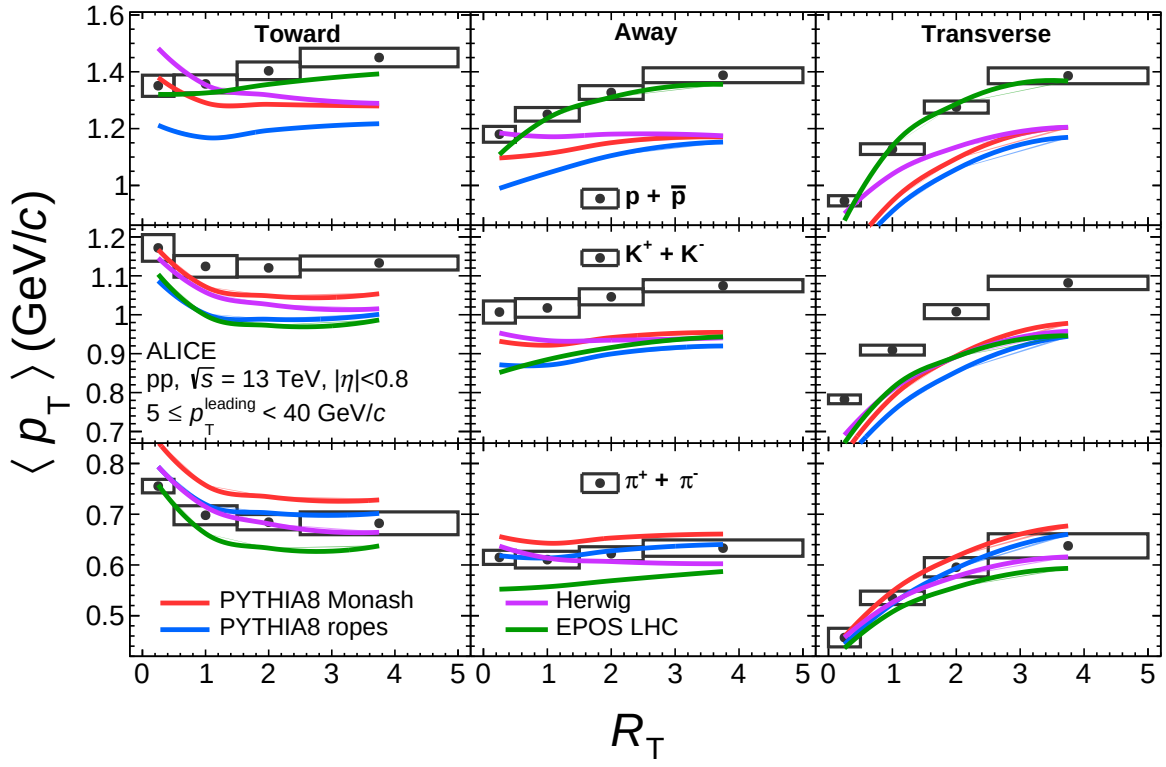

Figure 10: Average transverse momentum as a function of R_{T}. The $\langle p_{\mathrm{T}} \rangle$ in the toward, away, and transverse regions are shown from left to right. The results for pion, kaon, and protons are shown in the first, second, and third row, respectively. Statistical and systematic uncertainties are represented with error bars and boxes, respectively. The shaded bands around the model lines represent the statistical uncertainties.

Figure 11 shows the R_{T}-dependence of the p_{T}-integrated particle ratios calculated from the extrapolated $\mathrm{d}N/\mathrm{d}y$. As the UE activity increases, the yield of kaons and protons relative to that of pions increases in the transverse region and in turn, the particle ratios grow until they saturate at $R_{\mathrm{T}} \approx 1.5$. In contrast, in the toward and away regions the K/π ratio is constant as a function of R_{T}, while the p/π ratio decreases with increasing UE activity. Furthermore, both ratios in the toward and away regions approach the values of the transverse region at large R_{T}. All models predict the increasing trend of the particle ratios with R_{T} in the transverse region. PYTHIA8 Monash and Herwig predict similar p/π ratios to the data. PYTHIA8 ropes misses the p/π by a large amount (almost a factor of 2) while EPOS LHC, although overpredicting, is closer to the data. One can notice that while EPOS LHC precisely describes the proton $\langle p_{\mathrm{T}} \rangle$ as a function of R_{T} in all the topological regions, the p/π ratio is only described in the low-UE limit ($0 \leq R_{\mathrm{T}} < 0.5$), where string fragmentation dominates, indicating that the core overestimates the production of protons. PYTHIA8 Monash overpredicts the p/π ratio by about 10 % over the entire R_{T} range and underestimates the K/π ratio. In the toward and away regions none of the models gets the trend of both ratios: Herwig and PYTHIA8 Monash predict a strongly decreasing trend for K/π that is not supported by the data. PYTHIA8 ropes and EPOS LHC predict an increasing trend for p/π that is in contradiction with the data. Finally, it is noted that while all the models capture most of the measured trends for $\langle p_{\mathrm{T}} \rangle$ in Fig. 10, none of the models describes the particle ratio trends of Fig. 11 for both p/π

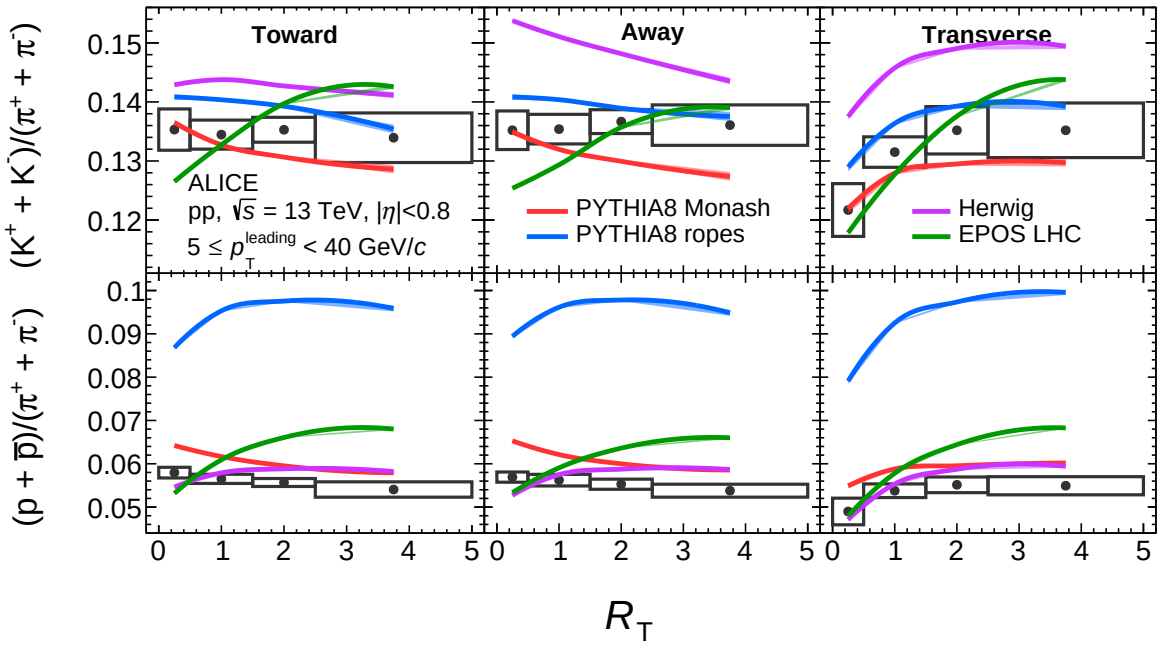

Figure 11: Transverse momentum-integrated particle ratios as a function of R_{T}. The particle ratios in the toward, away, and transverse regions are shown from left to right. The top (bottom) row plots the p/π (K/π). The statistical and systematic uncertainties are represented with error bars and boxes, respectively. The shaded bands around the model lines represent the statistical uncertainties.

and K/π.

5 Conclusions

The production of π, K, and p was measured at mid-pseudorapidity in different topological regions as a function of the relative transverse activity classifier, R_{T} in pp collisions at $\sqrt{s} = 13$ TeV containing a high p_{T} ($5 \leq p_{\mathrm{T}}^{\mathrm{leading}} < 40$ GeV/c) leading particle. R_{T} has been utilised to investigate differentially in different topological regions where the particle production is expected to be dominantly driven by pQCD-like processes (toward and away regions and low R_{T}) and regions where soft non-perturbative QCD processes dominate (transverse region or high R_{T}). In particular, since conventional UE (Underlying Event) studies average over the event activity, this analysis allows us to get further insight into collective effects and the interplay between hard and soft production in pp collisions. Furthermore, the models can describe the new results in the toward and away regions when the UE is suppressed ($0 \leq R_{\mathrm{T}} < 0.5$), which was expected since they are tuned to reproduce jet-like $\mathrm{e}^{+}\mathrm{e}^{-}$ measurements. However, when the UE increases, all models fail to reproduce the data at both qualitative and quantitative level. This demonstrates that by measuring the production of identified particles as a function of R_{T}, one can reveal novel features of the UE. The new measurements presented here thus allow for substantial progress on the model side to nail down the properties of the UE.

References

[1] **CMS** Collaboration, V. Khachatryan *et al.*, "Multiplicity and rapidity dependence of strange hadron production in pp, pPb, and PbPb collisions at the LHC", *Phys. Lett. B* **768** (2017) 103–129, arXiv:1605.06699 [nucl-ex].

[2] **ALICE** Collaboration, S. Acharya *et al.*, "Multiplicity dependence of light-flavor hadron production in pp collisions at $\sqrt{s} = 7$ TeV", *Phys. Rev. C* **99** (2019) 024906, arXiv:1807.11321 [nucl-ex].

[3] **ALICE** Collaboration, S. Acharya *et al.*, "Multiplicity dependence of π, K, and p production in pp collisions at $\sqrt{s} = 13$ TeV", *Eur. Phys. J. C* **80** (2020) 693, arXiv:2003.02394 [nucl-ex].

[4] **ALICE** Collaboration, B. B. Abelev *et al.*, "Multiplicity Dependence of Pion, Kaon, Proton and Lambda Production in p–Pb Collisions at $\sqrt{s_{\mathrm{NN}}}$ = 5.02 TeV", *Phys. Lett. B* **728** (2014) 25–38, arXiv:1307.6796 [nucl-ex].

[5] **CMS** Collaboration, V. Khachatryan *et al.*, "Evidence for collectivity in pp collisions at the LHC", *Phys. Lett. B* **765** (2017) 193–220, arXiv:1606.06198 [nucl-ex].

[6] **ALICE** Collaboration, S. Acharya *et al.*, "Investigations of Anisotropic Flow Using Multiparticle Azimuthal Correlations in pp, p–Pb, Xe–Xe, and Pb–Pb Collisions at the LHC", *Phys. Rev. Lett.* **123** (2019) 142301, arXiv:1903.01790 [nucl-ex].

[7] **ALICE** Collaboration, S. Acharya *et al.*, "Multiplicity dependence of (multi-)strange hadron production in proton-proton collisions at $\sqrt{s} = 13$ TeV", *Eur. Phys. J. C* **80** (2020) 167, arXiv:1908.01861 [nucl-ex].

[8] **ALICE** Collaboration, J. Adam *et al.*, "Enhanced production of multi-strange hadrons in high-multiplicity proton-proton collisions", *Nature Phys.* **13** (2017) 535–539, arXiv:1606.07424 [nucl-ex].

[9] **CMS** Collaboration, A. M. Sirunyan *et al.*, "Measurement of charged pion, kaon, and proton production in proton-proton collisions at $\sqrt{s} = 13$ TeV", *Phys. Rev. D* **96** (2017) 112003, arXiv:1706.10194 [hep-ex].

[10] T. Martin, P. Skands, and S. Farrington, "Probing Collective Effects in Hadronisation with the Extremes of the Underlying Event", *Eur. Phys. J. C* **76** (2016) 299, arXiv:1603.05298 [hep-ph].

[11] T. Sjostrand, S. Mrenna, and P. Z. Skands, "A Brief Introduction to PYTHIA 8.1", *Comput. Phys. Commun.* **178** (2008) 852–867, arXiv:0710.3820 [hep-ph].

[12] M. Bahr *et al.*, "Herwig++ Physics and Manual", *Eur. Phys. J. C* **58** (2008) 639–707, arXiv:0803.0883 [hep-ph].

[13] J. Bellm *et al.*, "Herwig 7.0/Herwig++ 3.0 release note", *Eur. Phys. J. C* **76** (2016) 196, arXiv:1512.01178 [hep-ph].

[14] A. Ortiz, G. Bencedi, and H. Bello, "Revealing the source of the radial flow patterns in proton–proton collisions using hard probes", *J. Phys. G* **44** (2017) 065001, arXiv:1608.04784 [hep-ph].

[15] **ALICE** Collaboration, E. Abbas *et al.*, "Mid-rapidity anti-baryon to baryon ratios in pp collisions at $\sqrt{s} = 0.9$, 2.76 and 7 TeV measured by ALICE", *Eur. Phys. J. C* **73** (2013) 2496, arXiv:1305.1562 [nucl-ex].

[16] **ALICE** Collaboration, S. Acharya *et al.*, "Underlying Event properties in pp collisions at $\sqrt{s}$ = 13 TeV", *JHEP* **04** (2020) 192, arXiv:1910.14400 [nucl-ex].

[17] **ATLAS** Collaboration, G. Aad *et al.*, "Measurement of the underlying event in jet events from 7 TeV proton-proton collisions with the ATLAS detector", *Eur. Phys. J. C* **74** (2014) 2965, arXiv:1406.0392 [hep-ex].

[18] **CDF** Collaboration, T. Affolder *et al.*, "Charged jet evolution and the underlying event in proton-antiproton collisions at 1.8 TeV", *Phys. Rev. D* **65** (Apr, 2002) 092002.

[19] A. Ortiz, G. Paić, and E. Cuautle, "Mid-rapidity charged hadron transverse spherocity in pp collisions simulated with Pythia", *Nucl. Phys. A* **941** (2015) 78–86, arXiv:1503.03129 [hep-ph].

[20] **ALICE** Collaboration, S. Acharya *et al.*, "Charged-particle production as a function of multiplicity and transverse spherocity in pp collisions at $\sqrt{s} = 5.02$ and 13 TeV", *Eur. Phys. J. C* **79** (2019) 857, arXiv:1905.07208 [nucl-ex].

[21] **ALICE** Collaboration, K. Aamodt *et al.*, "The ALICE experiment at the CERN LHC", *JINST* **3** (2008) S08002.

[22] **ALICE** Collaboration, B. B. Abelev *et al.*, "Performance of the ALICE Experiment at the CERN LHC", *Int. J. Mod. Phys. A* **29** (2014) 1430044, arXiv:1402.4476 [nucl-ex].

[23] **ALICE** Collaboration, E. Abbas *et al.*, "Performance of the ALICE VZERO system", *JINST* **8** (2013) P10016, arXiv:1306.3130 [nucl-ex].

[24] **ALICE** Collaboration, K. Aamodt *et al.*, "Alignment of the ALICE Inner Tracking System with cosmic-ray tracks", *JINST* **5** (2010) P03003, arXiv:1001.0502 [physics.ins-det].

[25] J. Alme *et al.*, "The ALICE TPC, a large 3-dimensional tracking device with fast readout for ultra-high multiplicity events", *Nucl. Instrum. Meth.* **A622** (2010) 316–367, arXiv:1001.1950 [physics.ins-det].

[26] A. Akindinov *et al.*, "Performance of the ALICE Time-Of-Flight detector at the LHC", *Eur. Phys. J. Plus* **128** (2013) 44.

[27] **ALICE** Collaboration, S. Acharya *et al.*, "Production of charged pions, kaons, and (anti-)protons in Pb–Pb and inelastic pp collisions at $\sqrt{s_{\mathrm{NN}}} = 5.02$ TeV", *Phys. Rev. C* **101** (2020) 044907, arXiv:1910.07678 [nucl-ex].

[28] **ALICE** Collaboration, J. Alme *et al.*, "The ALICE definition of primary particles",. https://cds.cern.ch/record/2270008.

[29] **ALICE** Collaboration, B. Abelev *et al.*, "Measurement of Event Background Fluctuations for Charged Particle Jet Reconstruction in Pb–Pb collisions at $\sqrt{s_{\mathrm{NN}}} = 2.76$ TeV", *JHEP* **03** (2012) 053, arXiv:1201.2423 [hep-ex].

[30] **ALICE** Collaboration, B. Abelev *et al.*, "Long-range angular correlations on the near and away side in p–Pb collisions at $\sqrt{s_{\mathrm{NN}}} = 5.02$ TeV", *Phys. Lett. B* **719** (2013) 29–41, arXiv:1212.2001 [nucl-ex].

[31] **ALICE** Collaboration, S. Acharya *et al.*, "Transverse momentum spectra and nuclear modification factors of charged particles in pp, p–Pb and Pb–Pb collisions at the LHC", *JHEP* **11** (2018) 013, arXiv:1802.09145 [nucl-ex].

[32] **ALICE** Collaboration, J. Adam *et al.*, "Centrality dependence of the nuclear modification factor of charged pions, kaons, and protons in Pb–Pb collisions at $\sqrt{s_{\mathrm{NN}}} = 2.76$ TeV", *Phys. Rev. C* **93** (2016) 034913, arXiv:1506.07287 [nucl-ex].

[33] **ALICE** Collaboration, B. B. Abelev *et al.*, "Production of charged pions, kaons and protons at large transverse momenta in pp and Pb–Pb collisions at $\sqrt{s_{\mathrm{NN}}} = 2.76$ TeV", *Phys. Lett. B* **736** (2014) 196–207, arXiv:1401.1250 [nucl-ex].

[34] **ALICE** Collaboration, J. Adam *et al.*, "Multiplicity dependence of charged pion, kaon, and (anti)proton production at large transverse momentum in p–Pb collisions at $\sqrt{s_{\mathrm{NN}}} = 5.02$ TeV", *Phys. Lett. B* **760** (2016) 720–735, arXiv:1601.03658 [nucl-ex].

[35] P. Skands, S. Carrazza, and J. Rojo, "Tuning PYTHIA 8.1: the Monash 2013 Tune", *Eur. Phys. J. C* **74** (2014) 3024, arXiv:1404.5630 [hep-ph].

[36] R. Brun, F. Bruyant, M. Maire, A. C. McPherson, and P. Zanarini, *GEANT 3: user's guide Geant 3.10, Geant 3.11; rev. version*. CERN, Geneva, 1987. https://cds.cern.ch/record/1119728.

[37] S. Agostinelli *et al.*, "Geant4-a simulation toolkit", *Nuclear Instruments and Methods in Physics Research Section A: Accelerators, Spectrometers, Detectors and Associated Equipment* **506** (2003) 250–303. https://www.sciencedirect.com/science/article/pii/S0168900203013688.

[38] A. Ferrari, P. R. Sala, A. Fassò, and J. Ranft, *FLUKA: A multi-particle transport code (program version 2005)*. CERN Yellow Reports: Monographs. CERN, Geneva, 2005. https://cds.cern.ch/record/898301.

[39] **ALICE** Collaboration, B. Abelev *et al.*, "Centrality dependence of π, K, p production in Pb–Pb collisions at $\sqrt{s_{\mathrm{NN}}} = 2.76$ TeV", *Phys. Rev. C* **88** (2013) 044910, arXiv:1303.0737 [hep-ex].

[40] G. D'Agostini, "A Multidimensional unfolding method based on Bayes' theorem", *Nucl. Instrum. Meth. A* **362** (1995) 487–498.

[41] T. Adye, "Unfolding algorithms and tests using RooUnfold", in *PHYSTAT 2011*. CERN, Geneva, 5, 2011. arXiv:1105.1160 [physics.data-an].

[42] T. Pierog, I. Karpenko, J. M. Katzy, E. Yatsenko, and K. Werner, "EPOS LHC: Test of collective hadronization with data measured at the CERN Large Hadron Collider", *Phys. Rev. C* **92** (2015) 034906, arXiv:1306.0121 [hep-ph].

[43] C. Bierlich, G. Gustafson, L. Lönnblad, and A. Tarasov, "Effects of Overlapping Strings in pp Collisions", *JHEP* **03** (2015) 148, arXiv:1412.6259 [hep-ph].

[44] S. Gieseke, P. Kirchgaeßer, and S. Plätzer, "Baryon production from cluster hadronisation", *Eur. Phys. J. C* **78** (2018) 99, arXiv:1710.10906 [hep-ph].

[45] T. Sjöstrand and M. van Zijl, "A multiple-interaction model for the event structure in hadron collisions", *Phys. Rev. D* **36** (Oct, 1987) 2019–2041. https://link.aps.org/doi/10.1103/PhysRevD.36.2019.

[46] T. Sjostrand, S. Mrenna, and P. Z. Skands, "PYTHIA 6.4 Physics and Manual", *JHEP* **05** (2006) 026, arXiv:hep-ph/0603175.

[47] A. Ortiz Velasquez, P. Christiansen, E. Cuautle Flores, I. Maldonado Cervantes, and G. Paić, "Color Reconnection and Flowlike Patterns in pp Collisions", *Phys. Rev. Lett.* **111** (2013) 042001, arXiv:1303.6326 [hep-ph].

[48] C. B. Duncan and P. Kirchgaeßer, "Kinematic strangeness production in cluster hadronization", *Eur. Phys. J. C* **79** (2019) 61, arXiv:1811.10336 [hep-ph].

[49] **ALICE** Collaboration, S. Acharya *et al.*, "Production of Λ and $\mathrm{K}^0_{\mathrm{S}}$ in jets in p–Pb collisions at $\sqrt{s_{\mathrm{NN}}} = 5.02$ TeV and pp collisions at $\sqrt{s} = 7$ TeV", *Phys. Lett. B* **827** (2022) 136984, arXiv:2105.04890 [nucl-ex].

[50] C. Tsallis, "Possible generalization of boltzmann-gibbs statistics", *Journal of statistical physics* **52** (1988) 479–487.

[51] G. Wilk and Z. Wlodarczyk, "On the interpretation of nonextensive parameter q in Tsallis statistics and Levy distributions", *Phys. Rev. Lett.* **84** (2000) 2770, arXiv:hep-ph/9908459.